Science Advances
AAAS

Supplementary Materials for

Flexible multichannel muscle impedance sensors for collaborative human-machine interfaces

Junwei Li *et al.*

Corresponding author: Yifan Wang, yifan.wang@ntu.edu.sg

Sci. Adv. **11**, eadv3359 (2025)
DOI: 10.1126/sciadv.adv3359

The PDF file includes:

Supplementary Text
Notes S1 to S9
Tables S1 and S2
Figs. S1 to S12
Legends for movies S1 to S4

Other Supplementary Material for this manuscript includes the following:

Movies S1 to S4

Note S1. Tensile test on the modified PDMS layer.

Fig. S2 shows the results of a tensile test performed on the modified PDMS layer, with the shaded area representing the standard deviation. The elastic modulus, calculated from the slope in the 0-83% strain range, is 212.8 kPa.

Note S2. Electrical-impedance-measurement simulation protocol.

The commercial finite-element software COMSOL was used to simulate the electrical impedance measurement on human forearm. Given that the electrode array is pasted around the cross-section of forearm and the main electric streamline flows within this cross section, a two-dimensional model was used for simplifying and accelerating the simulation. The geometry of the forearm is extracted using machine-vision digitalizing method based on the anatomy figure provided in (*33*), as shown in Fig. S3. The electric currents module in COMSOL was used to simulate current stimulation and voltage measurement. The electrical conductivities and relative permittivities of different tissues at 50kHz are summarized in Table S1 (*34*).

Note S3. Analysis of signal-to-noise ratios for different measurement configurations

The impedance features measured using the different configurations exhibit varying sensitivity to electrode movement, resulting in different noise levels. Here, we use numerical simulations to compare two categories of measurement configurations: one where the measurement electrodes are shared with the stimulating loop, and another where independent measurement electrodes are used. The simulations were performed using the solid mechanics and electric currents modules in COMSOL software.

Fig. S4A illustrates a configuration where a sinusoidal current (amplitude of 0.4 mA and frequency of 50 kHz) is applied to the tissue through the seventh and tenth electrodes. Due to the mismatch between the flexible electrode pad and human skin, unavoidable movement occurs both at the current-input electrodes (e.g., electrode #10) and at other electrodes (e.g., electrode #9). When a movement of 0.8 mm occurred at electrode #10 or #9, the stress around the electrode increased (as shown by the von Mises stress in Fig. S4B), leading to an increase in contact-surface conductivity, which in turn affected the measured voltages. The relationship between contact-surface conductivity and contact force was modeled as a linear correlation, as shown in Fig. S4C. Using this correlation, movement artifacts (voltage changes due to electrode movement) were simulated and are displayed in Fig. S4D. In the first two configurations shown in Fig. S4D, electrode movement caused relatively large voltage fluctuations. However, in the last configuration, known as four-point measurement, movements of both the current-input and measurement electrodes had minimal impact on the voltage. These simulations suggest that the four-point measurement configuration offers a better signal-to-noise ratio due to its reduced sensitivity to contact impedance changes.

Note S4. Performance metrics of FMEIS

The detection depth, motion artifact rejection ability, detection resolution, cost, and compatibility of four different types of methods—electromyography (EMG), ultrasound imaging, magnetic sensing, and electrical impedance sensing (this work)—are discussed here.

The detection depths of the first three methods are summarized based on a review of relevant literature (Table S2). The detection depth of electrical impedance sensing (this work) is primarily influenced by stimulation frequency, current amplitude, electrode spacing, and hardware noise level. We selected 50 kHz as the current injection frequency because, at this frequency, the conductivity of skin and fat is sufficiently high for current penetration into deeper muscle regions (*23, 25, 34*). Additionally, the chosen current amplitude (0.4 mA) was comfortable for all subjects, generating virtually no sensation, while still providing a favorable signal-to-noise ratio. Thus, we focused on analyzing the effects of electrode spacing and hardware noise levels on the detection depth of FMEIS using both numerical simulations and experimental validations. A finite-element analysis of the impedance detection process was performed following the simulation protocol described in Note S2, utilizing electrical properties listed in Table S1. To minimize interference from variations in biological tissue geometry during depth analysis, we adopted a simplified geometric model consisting of an outer layer (skin and fat) and inner structures (muscle and bone), as illustrated in Fig. S6A. The impedance change associated with muscle contraction was simulated by adjusting the conductivity of a target muscle from 0.3 S/m (initial) to 0.24 S/m (contracted), based on previously published experimental data (*23*). The distance from the center of this target muscle to the skin surface is defined as the target depth D. The 16-channel FMEIS sensor was positioned above the target muscle, with neighboring electrode spacing identical to the physical FMEIS sensor (6.5 mm). For various target depths D ranging from 15 mm (muscle close to the skin surface) to 45 mm (muscle at the center of the forearm), different electrode pairs with varying distances (Fig. S6A) were employed to inject a current of 0.4 mA at 50 kHz for impedance sensing.

The resulting electrical potential changes across all electrodes, reflecting simulated muscle contractions, are presented in Fig. S6B. Given that the voltage sampling module used in the wired hardware version has a resolution of 0.3 mV, the noise region for sampled voltage changes was set to ±0.3 mV (highlighted by orange shading in Fig. S6B), as experimentally confirmed in Fig. S7. As shown in Fig. S6B, when the target muscle was at a greater depth (D = 45 mm), the electric potential changes recorded by all electrode pairs fell within the noise range, yielding unreliable results. At shallower depths, electrode pairs with greater spacing effectively detected potential changes indicative of muscle contractions. Taking the target depth of D = 35 mm as an example, the first five current-injection patterns produced potential changes at least twice the magnitude of the noise region. To quantify the relationship between electrode spacing and detection depth, the electrode pairs most sensitive to different muscle depths are marked with 'L' in Fig. S6B. The distribution of these sensitive pairs demonstrates a proportional relationship between detection

depth and electrode spacing. For instance, a wide electrode pair (2, 15) effectively detected muscle contraction at $D = 40$ mm, while a narrower electrode pair (6, 11) was optimal for detecting muscle contraction at $D = 15$ mm. Based on this analysis and considering the actual depth range of forearm muscles, we selected a current-injection pair with a spacing of seven electrodes (e.g., electrodes 1 and 9) to detect both superficial and deeper muscles. According to the simulation results (Fig. S6B), this electrode pair provides an effective detection depth of approximately 35 mm.

From an experimental perspective, we evaluated the capability of FMEIS to detect various hand gestures actuated by muscles located at different depths (Movie S1, Fig. S7). The FMEIS was attached to the medial side of the forearm. For each gesture, the locations of actuating muscles were determined through anatomical landmarks and visible skin deformation. Subsequently, a four-point impedance measurement was performed using a pair of electrodes positioned above the target muscle with a spacing of seven electrodes, along with their two inner neighboring electrodes. The ability of impedance measurements to reflect muscle contractions is demonstrated in Movie S1 and Fig. S7. The impedance curves in Fig. S7 clearly show the detection of all gestures and corresponding muscle contractions (muscles listed in Fig. S7 caption). According to anatomical references for these muscles (*33*), their depths range from 8 to 30 mm. The experimentally demonstrated maximum detection depth of approximately 30 mm closely aligns with the numerical simulation result of around 35 mm. Notably, the detection depth of 35 mm is sufficient for forearm muscle monitoring, as the depths of forearm muscles typically fall within this range.

The motion artifact rejection capabilities of the compared methods are quantified by considering both the elastic modulus of the probe heads and the adhesive force between the probes and the skin. We use the 90° peeling force from the skin to quantify adhesive strength. Notably, the proposed FMEIS sensor exhibits the lowest elastic modulus and a moderate adhesive force (12.73 N/m). Moreover, the adhesive interface is reusable due to the presence of reversible hydrogen bonds, as illustrated in Fig. 2D. These features contribute to the FMEIS's excellent ability to reject motion artifacts. For detection resolution, we use the number of independent signals that can be acquired with 16 probes, as the minimum detectable feature size is mathematically and directly related to this number (*54*). Both the ultrasound method (*19*) and FMEIS can utilize an embedded multiplexer to dynamically select transmitting and receiving probes from the total of 16, yielding up to 120 independent measurements based on the reciprocity theorem in electric and acoustic fields (*53, 54*). In contrast, for EMG and magnetic sensing methods, the number of independent signals is limited to the number of probes used. Therefore, under the same probe count, FMEIS can achieve a detection resolution comparable to that of the ultrasound method. The costs of the different methods are summarized based on publicly available quotations of their hardware components. Finally, as demonstrated in Fig. 5C, the FMEIS can operate alongside a commercial EMG sensor without interference. Since both are electric-field-based methods, they may even share electrodes in future implementations, demonstrating strong compatibility.

Note S5. Electrical impedance measurement setup.

In the opposite configuration (*35*), a pair of electrodes, such as the 1st and 9th electrodes in Fig. S8A, was used to inject a 50 kHz sinusoidal current. Using another electrode as the reference (e.g., the 2nd electrode in Fig. S8A), the electrical potentials of all other electrodes were measured sequentially, yielding 15 independent voltage signals. By applying the fast Fourier Transform (FFT) to these voltage signals and extracting their FFT amplitudes at 50 kHz (matching the source current), 15 impedance values were obtained. For eight different current-input configurations, a total of 120 independent impedance values were measured to analyze the tissue states. These 120 impedance values constituted an impedance pattern.

Note S6. Automatic feature selection using ANOVA and F-test

For hand gesture classification, one-way analysis of variance (ANOVA) (*36*) was used to extract the most representative features from the impedance pattern. This algorithm performs a one-way analysis of variance for each of the 120 impedance features (Fig. S8), grouping them by hand gestures, and then ranks the features based on their *p*-values. For each impedance feature, the algorithm tests the hypothesis that the impedance values grouped by hand gestures are drawn from populations with the same mean, against the alternative hypothesis that the population means are different. The importance scores of these features are defined as $-\log(p)$, with larger scores indicating higher importance. In the hand gesture classification tests, the top 91 impedance features with the highest importance scores were selected to achieve high classification accuracy.

For feature selection in muscle force regression, the importance of each impedance feature was evaluated using an *F*-test (*36*). Each *F*-test assesses the hypothesis that muscle force values grouped by impedance feature values are drawn from populations with the same mean, against the alternative hypothesis that the population means differ. The algorithm ranks the impedance features using the *p*-values of the *F*-test statistics by calculating the importance score $-\log(p)$. In the muscle force regression tests, the top 70 impedance features with the highest importance scores were selected to ensure good accuracy. Since fewer muscles were involved in the muscle force regression tests, fewer impedance features were relevant to muscle contractions.

It is also worth noting that both feature selection methods tended to automatically eliminate the impedance patterns measured using the first two configurations in Fig. S4D due to their higher noise levels, which resulted in lower importance scores.

Note S7. Machine learning models for gesture classification and muscle force regression

The structure of a single-hidden-layer neural network model used for hand gesture classification is illustrated by the schematic diagram in Fig. S9. The raw impedance pattern, consisting of 120 features (Supplementary Note S5), underwent a feature selection process (ANOVA in Supplementary Note S6) to extract an effective impedance pattern with 91 features. These features

were standardized to improve training performance. These selected features were then input into a fully connected hidden layer with 25 neurons. The ReLU activation function was employed in the hidden layer to introduce non-linearity into the model. The output layer consisted of 10 nodes, each representing one of the possible hand gestures (e.g., natural hand position, claw, wrist extension, wrist flexion). The model outputted the probability for each gesture, allowing the classification of the current hand gesture based on the impedance data. This configuration provided a balanced approach, ensuring reliable hand gesture classification without overfitting. The network was trained for up to 1000 iterations to ensure sufficient convergence.

For muscle force regression, we employed a quadratic support vector machine (SVM) model. The raw impedance pattern, consisting of 120 features (Supplementary Note S5), underwent a feature selection process (F-test in Supplementary Note S6) to extract an effective impedance pattern with 70 features. The selected 70 features were then input into the SVM model for predicting muscle force. The kernel function was set to quadratic, with the kernel scale and box constraint parameters automatically adjusted during training. Additionally, the epsilon parameter, which controls the width of the epsilon-insensitive region in the loss function, was set to auto. Data standardization was applied prior to training to ensure that all features had zero mean and unit variance, contributing to the improved performance of the model in force prediction tasks.

Note S8. Updating algorithm of incision process in VR surgery

In this VR surgery, the surgeon's hand movements, the motion of the surgical knife, and the deformation of the patient's skin were programmatically controlled based on real-time muscle force predicted by the fMEIS. On the virtual patient’s skin, a cutting path was pre-designed based on the surgical target. For example, in the case of gastric surgery, a cutting path would be pre-designed on the abdominal skin above the stomach. The position of the virtual surgical knife, which moved in sync with the surgeon's hand, and the surface morphology along the cutting path were updated at 60 frames per second based on the muscle force predictions from fMEIS. Whenever the real-world muscle force prediction exceeded 0, the virtual surgical knife advanced along the cutting path at a constant rate. The incision width at each point on the path was determined by the integral of the muscle force over a specified moving time window. This algorithm results in a cutting process that closely mirrors real-world conditions.

Note S9. Design schematics of wired and wireless versions of fMEIS sampling hardware

Fig. S11 shows the schematics and a picture of the wired-version fMEIS sampling hardware. The sensor pad is connected to the impedance sampling system. The system uses the WF3132 multiplexer to switch between different electrode pairs for both excitation and measurement. The CS580 current source receives the command from a signal generator and provides a stable sinusoidal excitation current to the electrodes, while the NI9223 voltage module samples the voltage across the selected electrodes at a high frequency (800 kHz). Both the multiplexer and voltage module are synchronized and controlled by the cRIO-9053 real-time controller, ensuring

accurate timing and data acquisition. The cRIO-9053 real-time controller also conduct on-board fast Fourier transform to convert the sinusoidal voltage signal to impedance pattern. The impedance pattern data is then transmitted to a computer, where machine-learning algorithms are applied for classification and regression tasks. This system setup allows real-time processing and analysis of the impedance measurements.

The wireless version of the impedance sampling hardware utilizes cost-effective chips and custom circuitry, providing high portability for the fMEIS. Fig. S12 shows the circuit schematics of the four parts of the wireless impedance sampling system, including the excitation current source (Fig. S12A), the analog voltage acquisition (Fig. S12B), the multiplexer (Fig. S12C), and the microcontroller along with the Bluetooth module (Fig. S12D). The picture of the wireless hardware can be found in Fig. 3A.

Table S1. Electrical properties of forearm tissues used in impedance measurement simulation.

	Skin	Fat	Fascia	Muscle	Bone
Conductivity (S/m)	0.3	0.2	0.39	0.3	0.03
Relative permittivity	20000	200	800	10000	600

Table S2. Performance metrics of different muscle-contraction detection methods.

Methods	Ref.	Detection depth	Motion artifact rejection		Resolution: Independent signal # using 16 probes	Cost: Price of wired hardware	Compatibility: Probe compatibility with other
			Probe elastic modulus	Peeling force			
EMG	(*9*)	< 15mm [12]	644 kPa	58 N/m (Not reusable)	16	~42,000 USD (16-channel Trigno Avanti, Delsys)	Compatible with this work
EMG	(*11*)	< 15mm [12]	~2GPa	~ 0, used commercial gel			
Ultrasound	(*19*)	160 mm (3MHz)	921 kPa	Nearly 0, need commercial adhesive	120	~102,000 USD (Vantage 32, Verasonics)	Not compatible
Ultrasound	(*21*)	66 mm (12MHz)	>1 GPa				
Magnetic	(*14*)	Invasive	>1 GPa	~ 0	16	<20,000 USD	Not compatible
This work	--	35 mm (50kHz)	212.8 kPa	12.73 N/m	120	~10,000 USD (16-channel)	Compatible with EMG

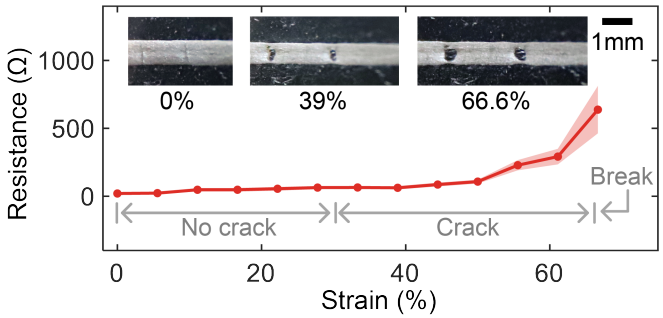


Fig. S1. Resistance changes of a conductive silver trace under varying strain. The three photos show the same silver trace under different strain levels.

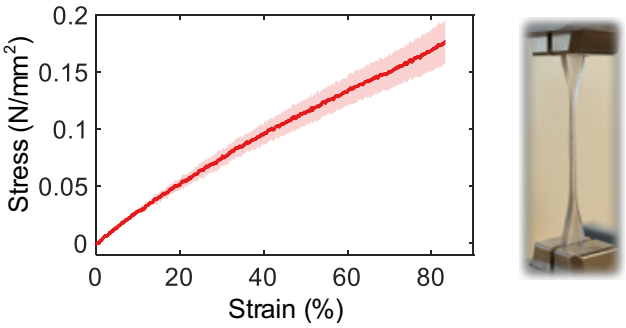


Fig. S2. Tensile test of modified PDMS layer showing the relation between its stress and strain.

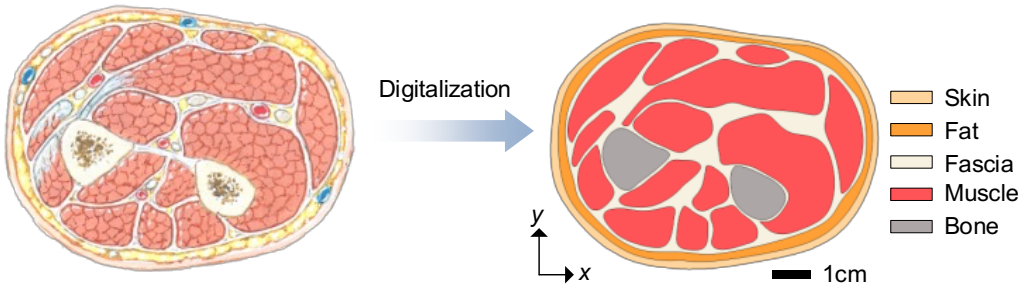


Fig. S3. Digitalization of anatomical figure to obtain tissue boundary-curve coordinates.

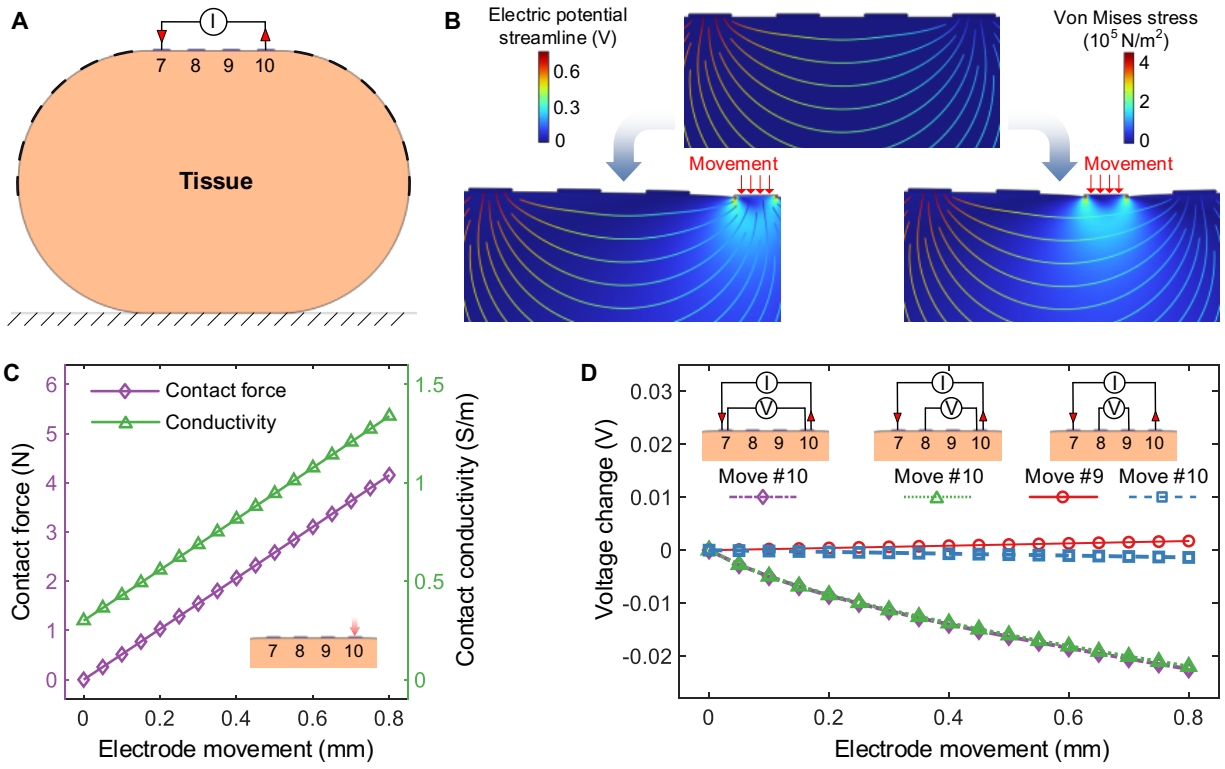


Fig. S4. Effects of electrode movements on impedance measurement. (**A**) One example of impedance measurement configuration. (**B**) Stress fields and electric potential streamlines when electrodes are subject to movements. (**C**) Contact force and contact conductivity under different electrode movements. (**D**) Voltage changes due to electrode movements under different configurations.

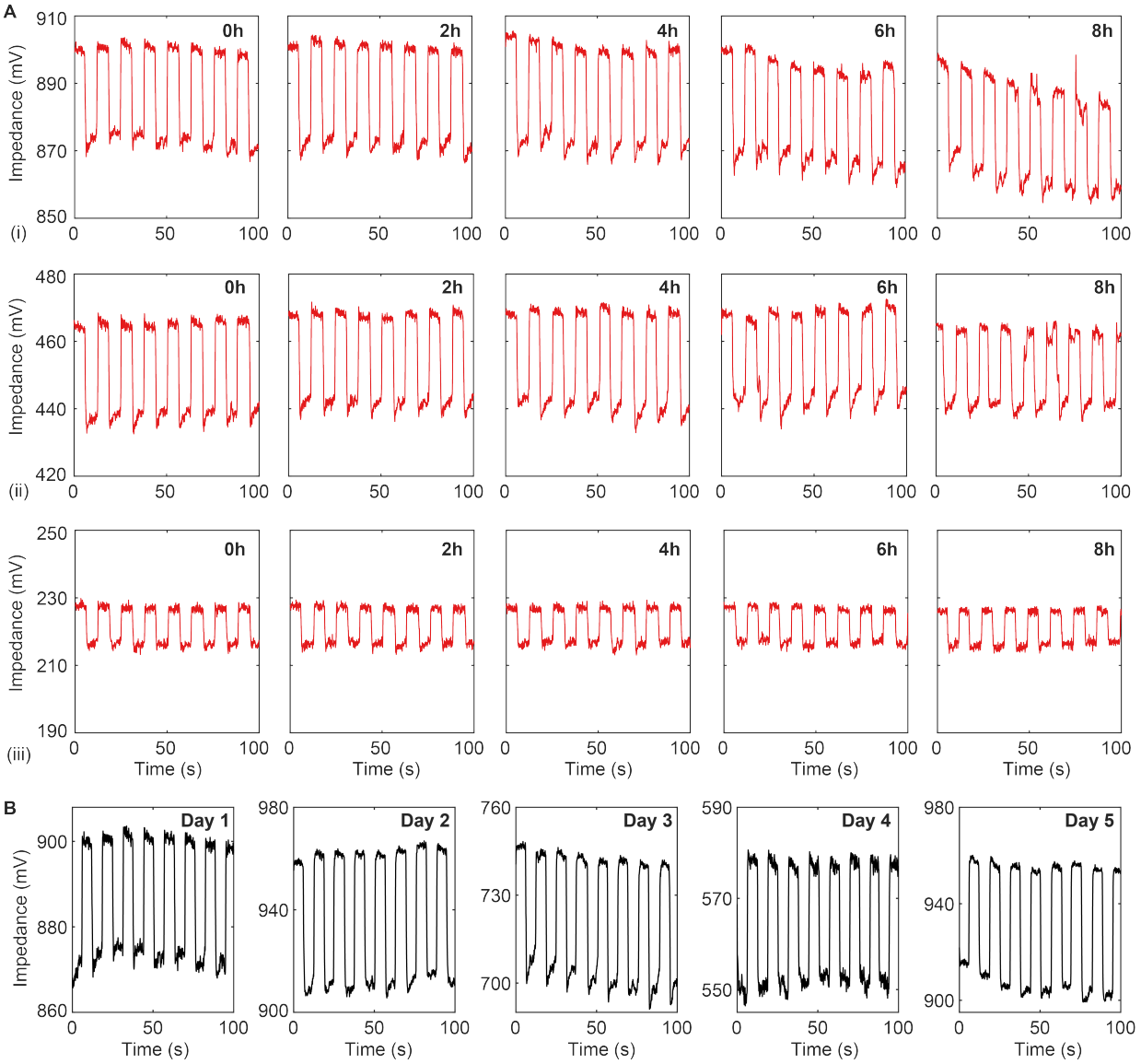


Fig. S5. Long-term stability and reusability analysis of FMEIS when electrodes 1 to 9 were positioned over the flexor digitorum superficialis (FDS). (**A**) Impedance signals recorded over 8 hours using three different electrode configurations (stimulation pair; measurement pair): (i) (1, 9; 2, 8), (ii) (1, 9; 3, 7), and (iii) (1, 9; 4, 6). (**B**) Impedance signals recorded over 5 days using configuration (1, 9; 2, 8), with hydrogel electrodes replaced daily. In both sets of experiments, the subject periodically performed natural/fist gestures to contract the FDS.

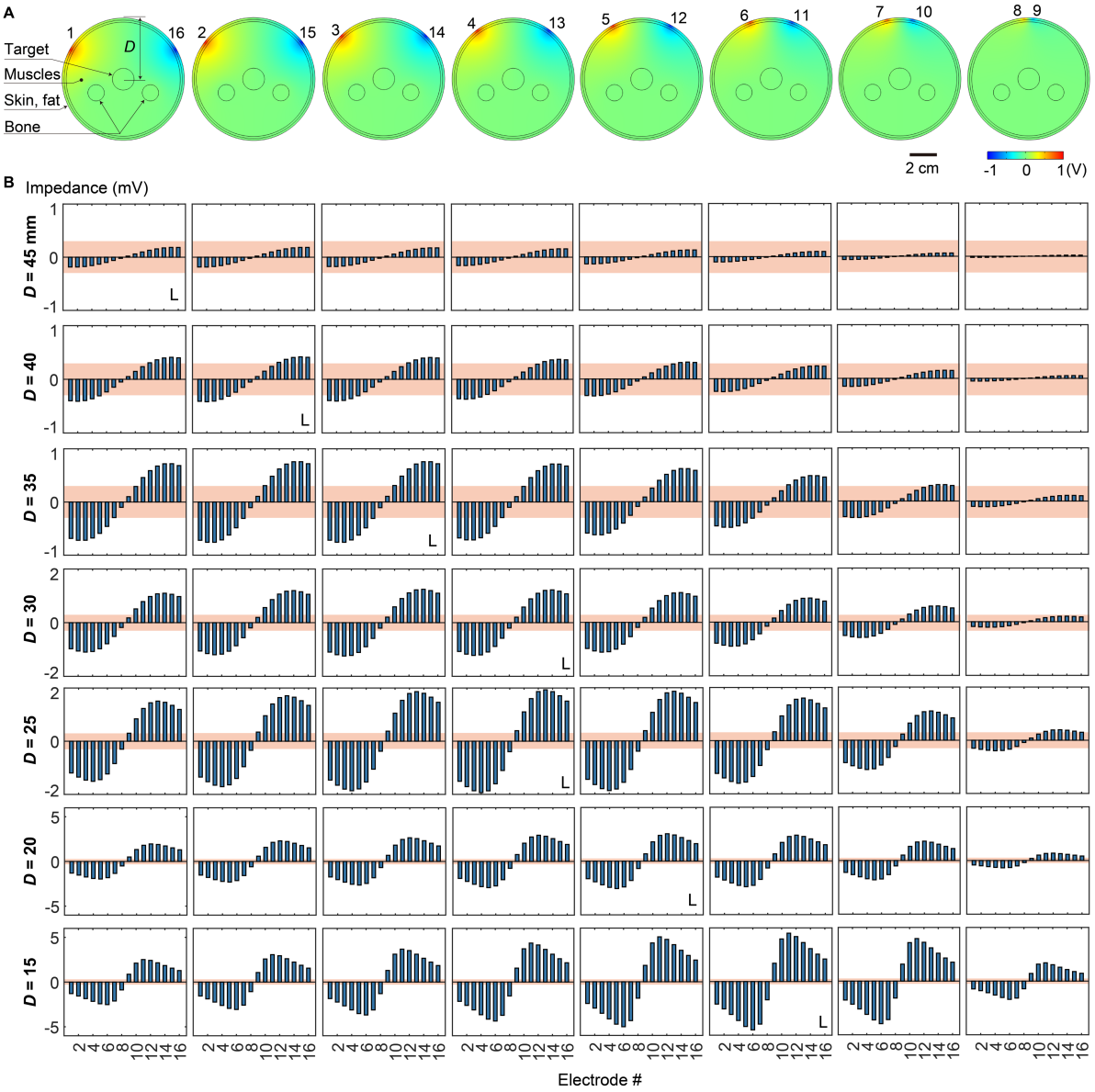


Fig. S6. Simulation of the detection depth for different impedance measurement configurations. (**A**) Electric fields for different current injection pairs. (**B**) Changes of electric potentials of 16 electrodes for different target muscle depths and different current injection pairs. The red shaded areas represent the noisy regions (with a width of 0.6mV) considering the resolution of the voltage sampling module (NI 9223) used in this work.

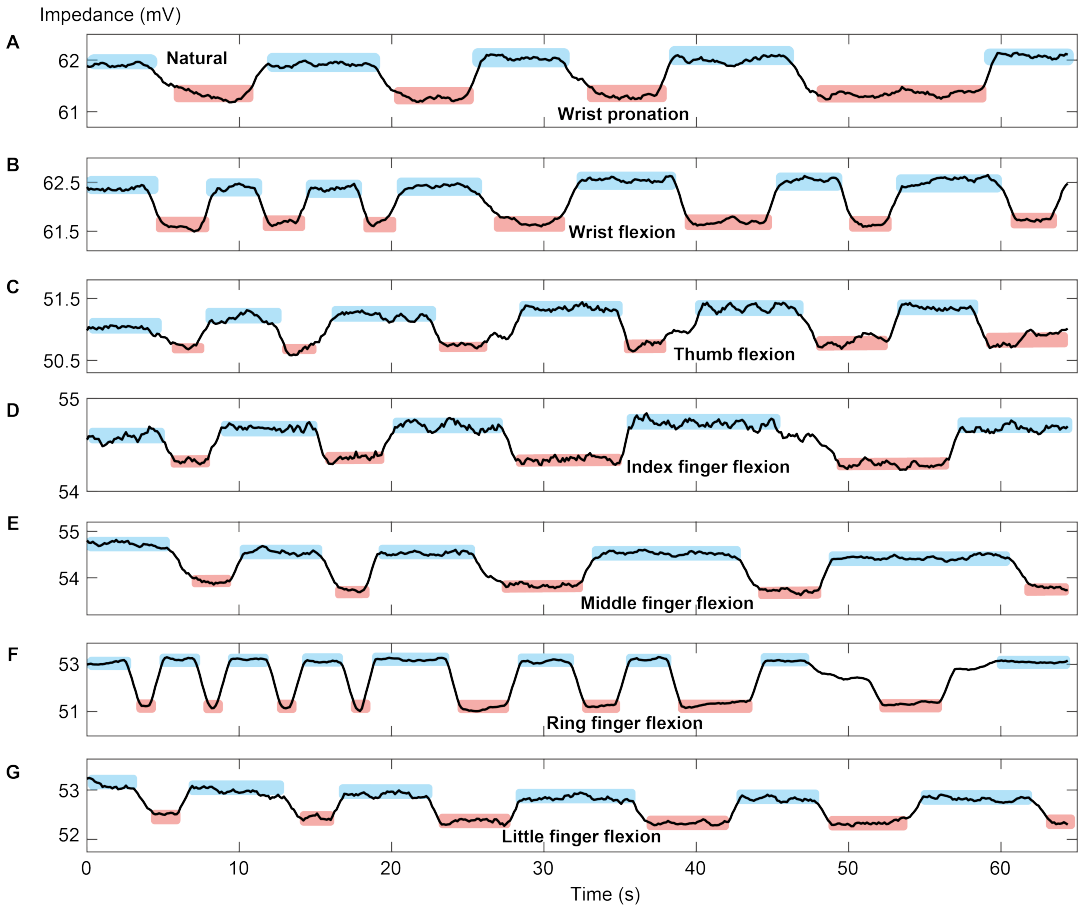


Fig. S7. Detection of various forearm motions recruiting muscles in different depths using FMEIS. (**A**) Wrist Pronation: pronator teres. (**B**) Wrist flexion: flexor digitorum superficialis, flexor carpi ulnaris, flexor carpi radialis, palmaris longus. (**C**) Thumb flexion: flexor pollicis longus. (**D**) Index finger flexion: flexor digitorum profundus. (**E**) Middle finger flexion: flexor digitorum profundus. (**F**) Ring finger flexion: flexor digitorum profundus. (**G**) Little finger flexion: flexor digitorum profundus.

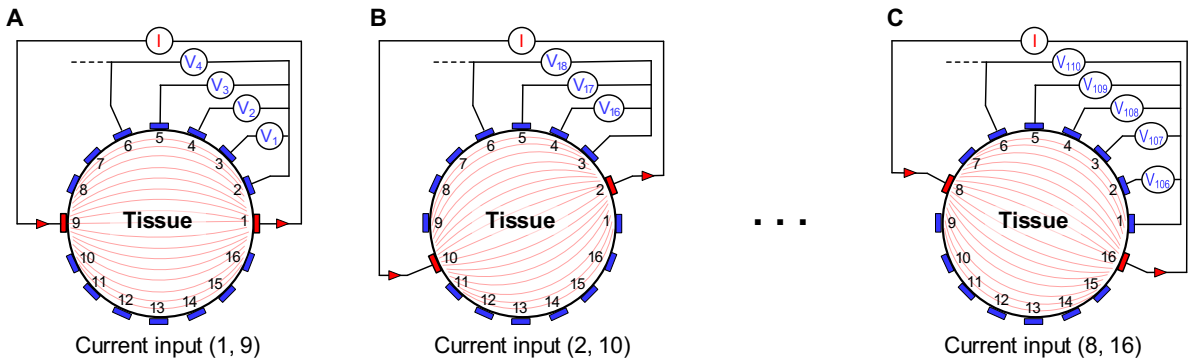


Fig. S8. All 120 independent impedance values in opposite configuration for 16 electrodes. (**A**) The first 15 impedance values for current input (1, 9). (**B**) The second 15 impedance values for current input (2, 10). (**C**) The last 15 impedance values for current input (8, 16).

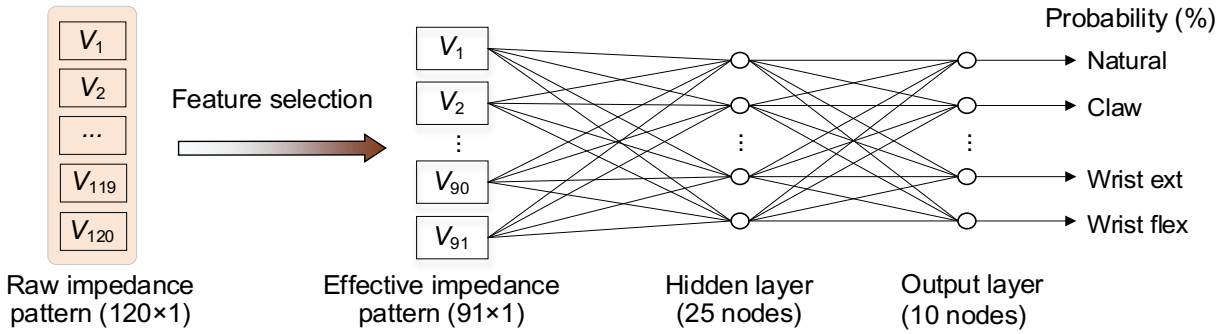


Fig. S9. Schematics of single-hidden-layer neural network model for hand gesture classification.

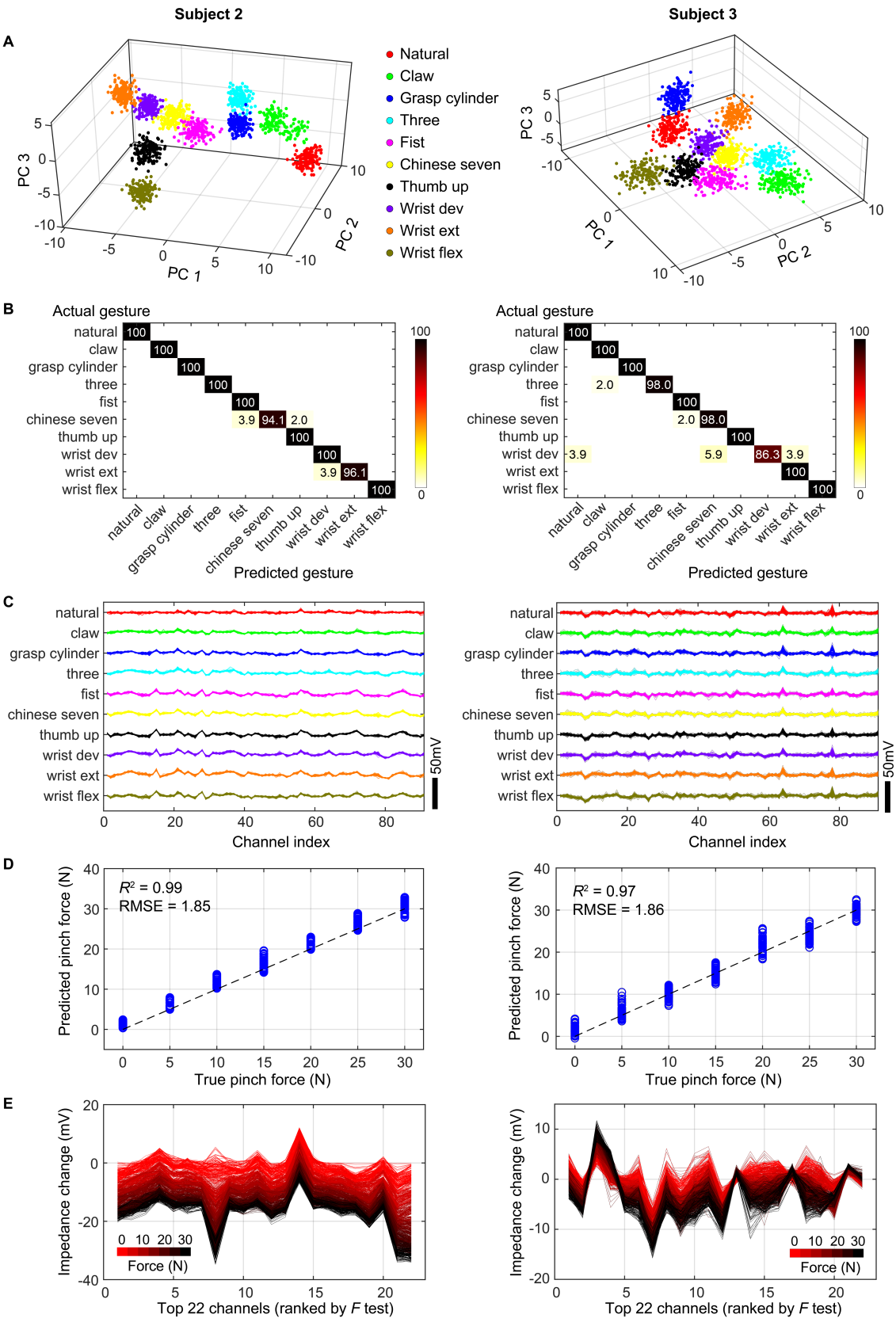


Fig. S10. Hand gesture classification and force regression results of Subject 2 and 3. (**A**) Three

dominant principal components (PC) of impedance pattern data for different hand gestures. Wrist (dev, ext, flex) represents wrist (deviation, extension, flexion). (**B**) Gesture prediction result using the muscle impedance data measuring by FMEIS. The overall accuracies for Subjects 2 and 3 are 99.02% and 98.24%, respectively. (**C**) Repeated impedance pattern data for all 10 gestures. The horizontal axis represents the channel number in impedance pattern. (**D**) Linear regression plot between the true and predicted pinch forces. (**E**) Impedance pattern data measured by FMEIS for 7 force levels. The horizontal axis represents the top 22 channels selected using *F*-test method.

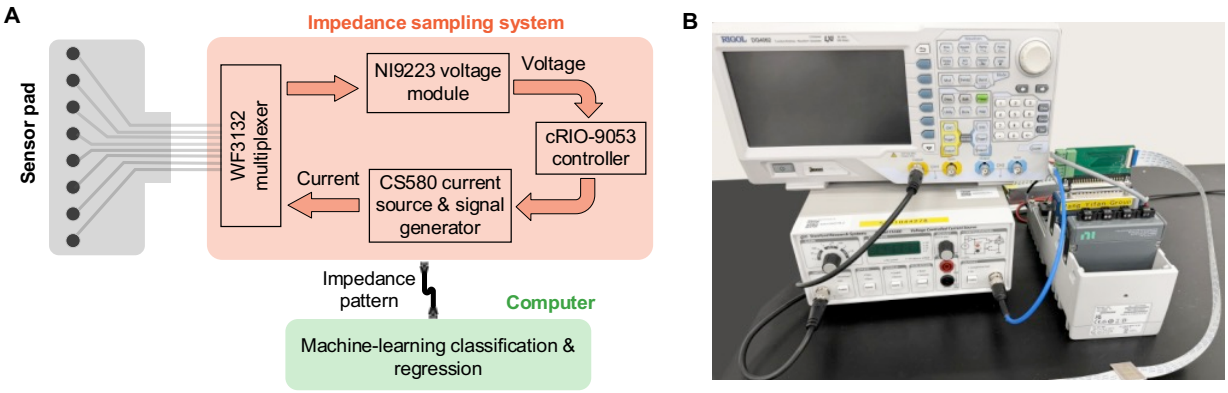


Fig. S11. Wired version of fMEIS sampling hardware. (**A**) Design schematics illustrating current injection, voltage acquisition, and impedance calculation. (**B**) Photo of the impedance sampling system in the wired version hardware.

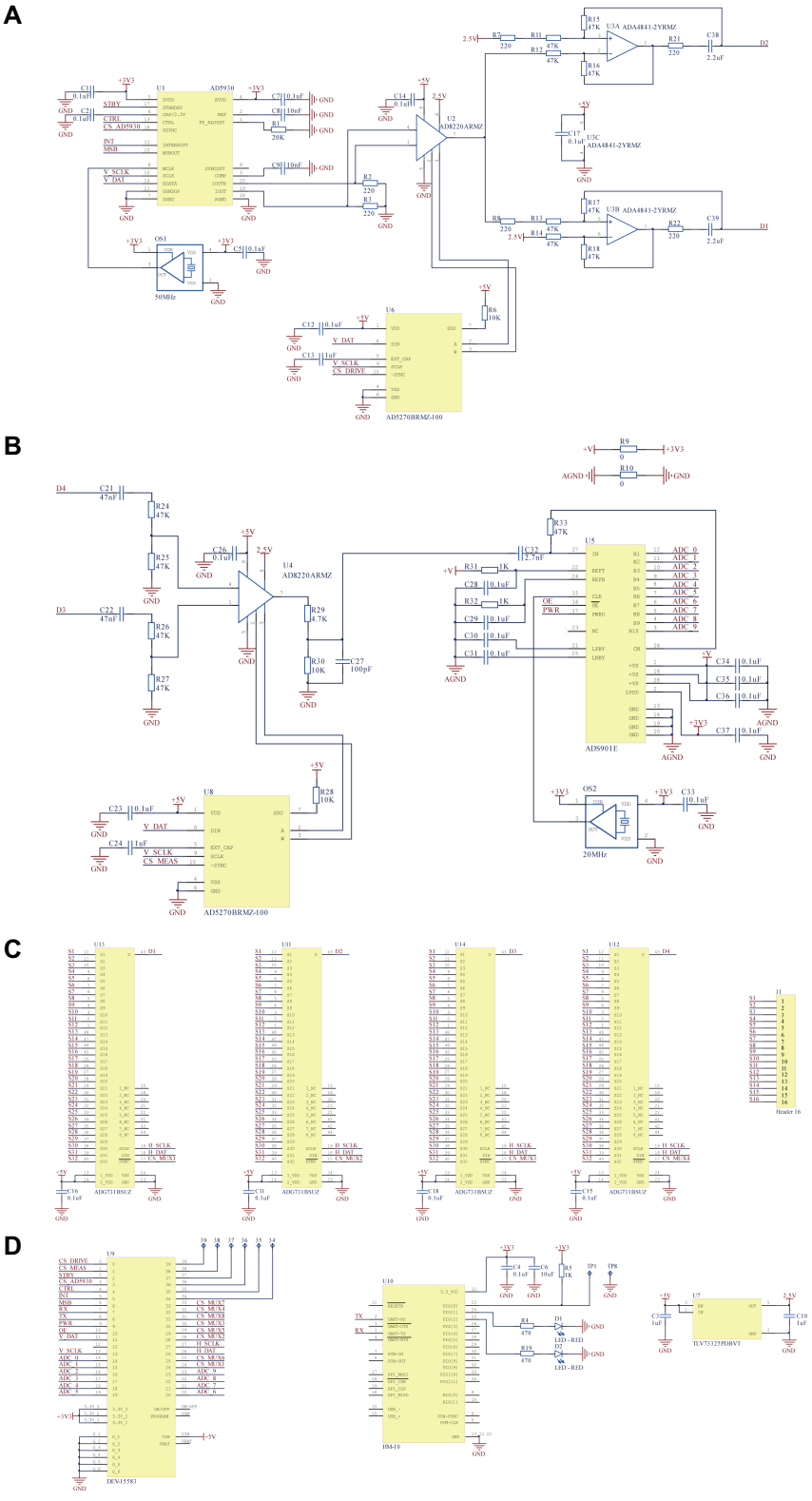


Fig. S12. Circuit schematic of wireless-version sampling PCB. The sub-schematics are the four functional parts: (**A**) Current source. (**B**) Voltage sampling. (**C**) Channel multiplexing. (**D**) Microcontroller and Bluetooth module.

Legends for Supplementary Movies

Movie S1. Demonstration of FMEIS detection range.
Movie S2. Robot motions controlled by human wearing FMEIS.
Movie S3. Human-robot collaboration using FMEIS.
Movie S4. VR surgery control based on measurements from FMEIS